JGR Planets

RESEARCH ARTICLE
10.1029/2025JE009585

Mercury's Tectonic and Geodynamic History: 2. Contribution of Membrane–Flexural Strains to the Tectonic Record

A. Broquet[1,2] **and J. C. Andrews-Hanna**[1]

[1]Lunar and Planetary Laboratory, University of Arizona, Tucson, AZ, USA, [2]Now at Institute of Space Research, German Aerospace Center, DLR, Berlin, Germany

Key Points:

- Lateral variations in membrane-flexural strain inverted from gravity and topography
- Membrane–flexural strains affect interpretations of the local tectonic record but have negligible effects on global contraction estimates
- Comparison to tectonic strain reveals long-lasting low-density mantle anomalies

Supporting Information:

Supporting Information may be found in the online version of this article.

Correspondence to:

A. Broquet,
adrien.broquet@dlr.de

Citation:

Broquet, A., & Andrews-Hanna, J. C. (2026). Mercury's tectonic and geodynamic history: 2. Contribution of membrane–flexural strains to the tectonic record. *Journal of Geophysical Research: Planets*, *131*, e2025JE009585. https://doi.org/10.1029/2025JE009585

Received 4 DEC 2025
Accepted 12 MAR 2026

Author Contributions:

Conceptualization: A. Broquet, J. C. Andrews-Hanna
Data curation: A. Broquet
Formal analysis: A. Broquet
Funding acquisition: A. Broquet, J. C. Andrews-Hanna
Investigation: A. Broquet
Methodology: A. Broquet, J. C. Andrews-Hanna
Project administration: A. Broquet, J. C. Andrews-Hanna
Resources: A. Broquet
Software: A. Broquet
Supervision: A. Broquet, J. C. Andrews-Hanna
Validation: A. Broquet, J. C. Andrews-Hanna
Visualization: A. Broquet
Writing – original draft: A. Broquet

Abstract Previous analyses of Mercury's tectonic record have arrived at widely varying amounts of global contraction. Contraction also varies spatially, with some regions displaying a near-zero record of contraction. Here, we investigate the contribution of membrane–flexural strain from lithosphere loading to the tectonic record. Using an inversion of present-day gravity and topography for Mercury's interior structure and lithosphere deformation, we show that membrane–flexural strain can counteract contractional strain as well as add to it. Long-wavelength support from the mantle systematically predicts flexural uplift and extension in the northern and Budh-Sobkou rises as well as the Caloris basin and the Otaared and Du Fu regions, thereby explaining their relative contractional tectonic strain deficit. This correlation indicates ancient, yet long-standing, support of topography in these regions, which must have been growing concurrently with the major phases of planetary contraction. Persistent compositional mantle anomalies or crustal underplating best explain such regional and long-lasting support. Although our models predict membrane–flexural compression in the northern smooth plains, contributing to the overconcentration of wrinkle ridges, neglecting the compressional tectonics there would underestimate the contractional strain. We constructed a novel inversion of gravity and topography using tectonic strain as a proxy for membrane–flexural deformations. This model self-consistently constrains Mercury's crust and mantle structure, also predicts the existence of long-standing and deep density anomalies, and explains Mercury's heterogeneous tectonic record. Future work must consider membrane–flexural strain as an important contribution to Mercury's regional tectonic records, which can both increase and decrease the local strain, but with a negligible net effect on global contraction.

Plain Language Summary Mercury's surface is populated by contractional tectonic features, which are the record of planetary cooling and shrinking over time. These features are not isotopically distributed, implying that some other processes have affected Mercury's tectonic history. Here, we invert present-day gravity and topography for Mercury's interior structure and lithosphere deformation in response to magmatic loading and mantle density variations. Long-wavelength support from the mantle systematically predicts flexural uplift and extension in the northern and Budh-Sobkou rises as well as the Caloris basin and the Otaared and Du Fu regions. This explains their relative contractional tectonic strain deficit and indicates ancient, yet long-standing, support of Mercury's topography in these regions. Although our models predict membrane–flexural compression in the northern smooth plain regions, which would contribute to the overconcentration of wrinkle ridges there, completely neglecting the compressional tectonics in this region would underestimate the contractional strain. We constructed a novel inversion of gravity and topography using tectonic strain as a proxy for membrane–flexural deformations. This model self-consistently constrains Mercury's crust and mantle structure, also predicts the existence of long-standing and deep density anomalies, and explains Mercury's heterogeneous tectonic record. Thus, future work must consider membrane–flexural strain as an important contribution to Mercury's regional tectonic records.

1. Introduction

Mercury's geodynamic evolution has been characterized by a long history of global contraction in response to cooling of the interior and growth of a solid inner core (Hauck et al., 2004; Knibbe & van Westrenen, 2018). A record of this protracted contraction history is preserved in the form of a global population of shortening landforms, including lobate scarps, high-relief ridges, and wrinkle ridges (e.g., Byrne et al., 2014; Crane & Klimczak, 2017; Watters, 2021). Different interpretations of Mercury's tectonic record led to distinct contraction

Writing – review & editing: A. Broquet, J. C. Andrews-Hanna

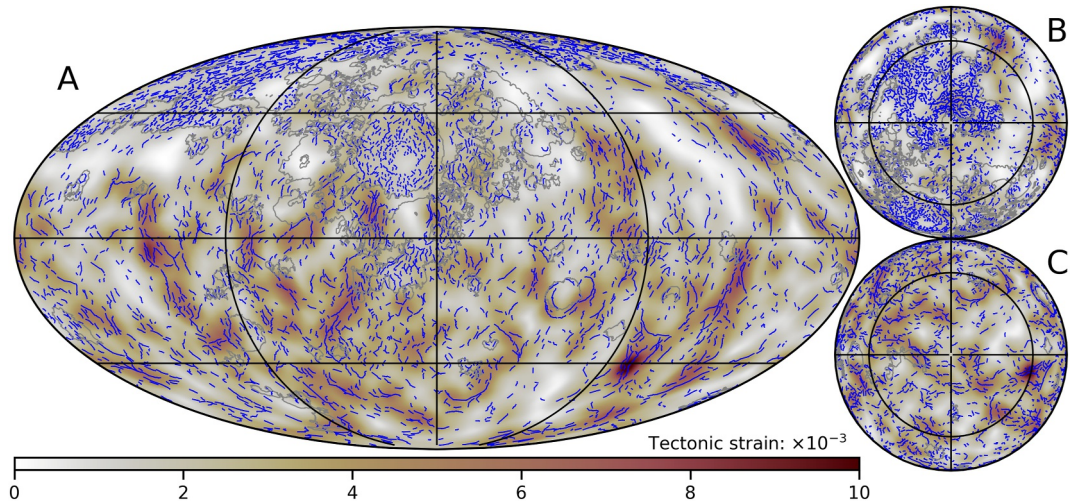

Figure 1. Mapped tectonic strain considering primary landforms in a Mollweide (a), north polar (b), and south polar (c) projection. The Mollweide map is centered on a longitude of 180°. For the geologic context, smooth plains are contoured in gray. Primary landforms were selected based on the tectonic catalog of Klimczak et al. (2025); see Broquet and Andrews-Hanna (2026) for more information.

estimates, with studies suggesting that the planet's radius has decreased by at most 1–2 km (Watters, 2021) or up to 7 km (Byrne et al., 2014; Crane & Klimczak, 2017; Di Achille et al., 2012). Proponents of the large contraction interpretation consider all tectonic landforms, including wrinkle ridges, as lithosphere-scale faults activated by global planetary contraction, while others interpret wrinkle ridges as arising from local deformations that do not reflect global contraction. In addition, studies have commonly used displacement-length ratios to estimate global contraction from catalogs of mapped landform segments (e.g., Byrne et al., 2014; Watters, 2021). However, it is unclear whether that approach can adequately infer tectonic strain and global contraction from tectonic databases that are subject to segmentation and where the shortening of individual faults might be overestimated with the mapping of secondary landforms (Watters, 2021).

In a companion paper (Broquet & Andrews-Hanna, 2026), we designed a neural network to extract the endpoints of a tectonic landform from an elevation profile orthogonal to the strike, and estimate the height of the shortening landform. This allows a robust estimation of tectonic strain accounting for segmentation as well as for the variability in height along a given tectonic landform. We further developed a primary landform selection approach to identify the dominant tectonic landform in areas in which shortening landforms are closely spaced or overlapping. This avoids the overestimation of tectonic strain in cases where multiple segments may be linked to a single large fault at depth. Finally, we proposed a formulation to estimate global contraction considering fault orientation, which improves upon assuming random or organized distributions. Applying this methodology to the tectonic catalog of Klimczak et al. (2025), we estimated the height of ∼53,000 tectonic segments and constrained that ∼6.3 km of global contraction is recorded by currently observable tectonic features.

An important observation in Broquet and Andrews-Hanna (2026) is that the mapped tectonic strain and associated contraction strongly vary with position (Figure 1; see also Watters et al. (2001, 2021), for example), with vast regions displaying near-zero tectonic strain ($<0.4 \times 10^{-3}$) compared to other locations with extreme tectonic strain concentration ($>10 \times 10^{-3}$). Such variations are at odds with the expectation of a globally and uniformly contracting planet from interior cooling and core crystallization and suggest that Mercury's tectonic record is either incomplete or was profoundly affected by other geodynamic processes.

A key outstanding question is to what extent strain from the loading and deformation of the lithosphere contributes to the tectonic record. Previous studies have investigated deformation processes including mascon loading (Kennedy et al., 2008), cooling of volcanic units (Freed et al., 2012), mantle flow and crustal loading (James et al., 2015; Watters et al., 2021), as well as planetary despinning (e.g., Klimczak et al., 2015; Matsuyama & Nimmo, 2009). In this work, we invert observed gravity and topography data collected by the MESSENGER mission (Solomon et al., 2007) to estimate the contribution of lithospheric loading and deformation to the tectonic

record. We consider different compensation mechanisms, including crustal loading and a combination of crustal and mantle loads (see also James et al., 2015), and compare lithosphere deformation patterns to the tectonic record described in Broquet and Andrews-Hanna (2026). A novel approach that uses tectonic strain to estimate membrane–flexural deformations and self-consistently infer Mercury's interior structure is also presented. Finally, we discuss what other factors might have contributed to the planet's heterogenous tectonic record.

2. Methods

2.1. Membrane–Flexural Strain From Gravity and Topography

Membrane–flexural strains experienced by Mercury's lithosphere and resulting from loading can be inverted from observed gravity and topography data (e.g., Andrews-Hanna et al., 2008; Broquet & Andrews-Hanna, 2023a; James et al., 2015). Our model solves for lithosphere deformation under the thin-elastic-shell assumptions, which are adequate for Mercury (e.g., Beuthe, 2008). Importantly, we note that loading in the model cannot induce a net global average deformation. Thus, the global average contractional tectonic strain should not be affected by superposed regional membrane–flexural strains.

The model inverts gravity and topography data for a combination of crustal loads applied at the surface, crustal loads applied at the crust-mantle interface, and loads from mantle density anomalies. Based on two observations (gravity and topography), it is possible to solve for only two forms of loading, such as crustal top and bottom loads, by setting the mantle load to zero (e.g., Andrews-Hanna & Broquet, 2023). Alternatively, by imposing additional constraints on the model, such as an isostatic relationship between the crustal top and bottom loads (Broquet & Andrews-Hanna, 2024), it is possible to solve for both crustal and mantle loads. Another option, which is explored below, is to assume that membrane–flexural deformations are fully reflected in the tectonic record. Regions with a tectonic strain excess (i.e., more predicted contractional strain compared to the average) can be interpreted as membrane–flexural subsidence, whereas regions with a deficit can be converted to membrane–flexural uplift. By prescribing membrane–flexural deformations, the inversion can fully characterize crustal and mantle loads. For more information on the inversion of gravity and topography data for a planet's interior structure and lithosphere deformation, we refer the reader to Banerdt (1986) (also e.g., James et al., 2015) and to our previous work (e.g., Broquet & Andrews-Hanna, 2023a; Broquet & Andrews-Hanna, 2024), as well as to our open-source code Displacement-strain-planet (DSP; Broquet, 2024).

Membrane–flexural strains strongly depend on the assumed compensation mechanism, and here we investigate two example scenarios. In one inversion, only crustal loading and lithospheric flexure are considered, with crustal top/bottom loads being constrained from gravity and topography. Such loads could arise from volcanic eruptions on the surface or volcanic underplating of the crust. This approach is similar to the single-layer model presented by James et al. (2015). In a second inversion, we use a combination of crustal and mantle loading, together with lithospheric flexure. Mercury's long-wavelength gravity and topography (degree <15), including the northern and Budh-Sobkou rises, are thought to be deeply compensated (James et al., 2015; Plattner & Johnson, 2021; Watters, 2021) and influenced by mantle dynamics and/or density anomalies (Tosi et al., 2015; Zuber et al., 2012). For that reason, this model assumes long-wavelength gravity and topography to result from an initially isostatic crust with crustal top/bottom loads in the isostatic ratio (providing negligible contribution to the gravity anomalies), combined with support from a variable density mantle. Shorter wavelengths are attributed to crustal loading only. The transition between both support regimes is defined by a cosine taper between degrees 10 and 20 and with an amplitude of 0.5 at degree 15 (half-wavelength resolution of 511 km; see Figure S1 in Supporting Information S1), consistent with previous work (James et al., 2015).

Inversions of gravity and topography are inherently non-unique, as the observed gravity and topography data can be reproduced for a continuum of assumed input parameters (see discussion below). However, they can still be used to estimate the extent to which membrane–flexural strains contribute to the tectonic record. As an example, our model does not consider the possibility that crustal loads originate from lateral variations in crustal density, although such models would also be consistent with observed gravity and topography data. In a lithospheric loading framework, whether the load originates from crustal thickness or density variations has little effect on the net load and associated displacement. The predicted strains for a model with crustal thinning/thickening would be comparable to those predicted by a model with variable crustal density. In addition, while previous studies have shown that Mercury's crustal composition varies laterally, the estimated grain density variations were found to be relatively small (± 150 kg m^{-3}, Beuthe et al., 2020) and would be insufficient to, alone, explain the planet's

heterogeneous gravity field. Crustal underplating and intrusions, the potential presence of a primary crust buried beneath the volcanically resurfaced crust, and porosity can lead to important crustal density variations that will affect the gravity field and the inferred crustal thickness (e.g., Broquet et al., 2024, 2025). However, these parameters and processes are not constrained on Mercury, and for simplicity, here we consider a constant-density crust.

In addition to the non-uniqueness, there are two main limitations of these models for Mercury. The first limitation deals with ancient deformations that are not recorded in the present-day topography and gravity field of Mercury. For example, past sequences of plume-induced deformation and flood volcanism can leave a substantial tectonic record of compression, while being mostly indiscernible in present-day gravity and topography data (e.g., Broquet & Andrews-Hanna, 2023a, 2023b). This point is further discussed in Section 4.

The second main limitation for Mercury is the resolution of the gravity field. Global gravity field solutions are reliable up to only about degree 10 (∼1,500 km wavelength) in the planet's southern hemisphere and extend to degree 90–160 in the north (∼100–170 km; Genova et al., 2023; Goossens et al., 2022). Compared to the gravity field, models of Mercury's topography are generally well constrained with a resolution of only several km across the planet (Becker et al., 2016). This difference in resolution effectively hinders our ability to determine the compensation state of the planet's relief at scales for which the gravity field is less resolved than topography. Thus, interior and crustal loads with wavelengths less than ∼1,500 km cannot be resolved in the southern hemisphere, although this region is affected by substantial short wavelength (∼500 km) variations in tectonic strain (Figure 1).

In order for our membrane–flexural strain inversion to not be biased by topographic loads unresolved in the gravity field of the southern hemisphere, while taking full advantage of the better data resolution in the northern hemisphere, we limit the spherical harmonic expansion of Mercury's topography to a spatially variable maximum spectral resolution (see also Broquet et al., 2024, 2025). For a function f with spatially variable spectral resolution L, this spectral degradation approach can be written as:

$$f(\theta,\phi) = \sum_{l=0}^{L(\theta,\phi)} \sum_{m=-l}^{l} f_{lm}\, Y_{lm}(\theta,\phi)$$

In this equation, θ is the co-latitude, ϕ is the longitude, and Y_{lm} is the spherical harmonic function of degree l and order m. In our case, the spatially variable spectral resolution is defined by the local gravity degree strength, which represents the degree at which the integrated gravitational acceleration uncertainty exceeds the Kaula rule (Genova et al., 2023; Konopliv et al., 2020). Topography data are obtained from a spherical harmonic expansion of a global digital elevation model (Becker et al., 2016), which is near error-free at gravity field resolution (wavelength >100 km). Gravity data is obtained from Genova et al. (2023), who applied a Kaula constraint to all degrees up to 160. We note that other choices of gravity model, including that of Konopliv et al. (2020) or Goossens et al. (2022), would have little influence on the presented results.

In all tested cases, we calculate a 2-D strain tensor from which we derive the principal strains (Banerdt, 1986). All of our strain maps show the magnitude of the areal strain at the surface, which is obtained by adding the sum of principal horizontal strains and their product.

2.2. Strain From Planetary Despinning

Mercury is currently rotating at a relatively slow 59-days frequency, leading to the existence of a small rotational bulge (Zuber et al., 2012). However, the rotation rate of the planet has likely changed over time and whether this phase of despinning occurred prior to or concurrent with Mercury's global contraction has implications for our estimates of the planet's geodynamic history (e.g., Beuthe, 2010; Klimczak et al., 2015).

In a simple case of planetary despinning, the degree-2 planetary displacement would induce thrust and strike-slip faulting in the equatorial area and normal faulting in the polar regions (Beuthe, 2010; Matsuyama & Nimmo, 2009). Thus, in the absence of true polar wander, despinning can contribute to thrust faulting in the equatorial areas, but will inhibit the formation of shortening landforms near the poles. Despinning also induces a net degree-0 displacement (uniform contraction) compressing the shell by a few tens of meters to several hundreds of meters, depending on the initial rotation rate. Such an effect is minor compared to Mercury's expected

global contraction, which exceeds several kilometers (e.g., Tosi et al., 2025). Importantly, while despinning alone might not provide sufficient stresses to induce faulting, its combination with global contraction may affect the tectonic fabric of Mercury (Klimczak et al., 2015).

If despinning was sufficiently early, stresses from despinning may have resulted in an early phase of tectonics that was subsequently erased by impacts or resurfacing events, and would not be observed today. In that case, the observed planetary degree-2 gravity and topography should be set to zero in our strain inversion for an adequate comparison to the tectonic record. Alternatively, if despinning occurs during planetary contraction, then the present-day gravity and topography signature of despinning (representing the fossil figure) should be used in the strain inversion. Given that Mercury's despinning is expected to have lasted during the major phases of global contraction (e.g., Matsuyama & Nimmo, 2009), the degree-2 gravity and topography are used in our membrane–flexural strain analysis. In addition, we note that work by Tosi et al. (2015) suggests that Mercury's long-wavelength gravity and topography (including the degree-2 terms) could be instead controlled by insolation-driven elastic deformations. Therein, Mercury's surface temperature pattern was also shown to propagate deep into the mantle, causing mantle temperature/density anomalies that are fully consistent with the planet's long-wavelength topography and geoid. In that case, the degree-2 gravity and topography should also be used in the inversion, assuming they are the result of mantle density anomalies rather than crustal loading. Thus, in this work, the degree-2 gravity and topography are considered as loads when inferring membrane–flexural strains.

2.3. Input Parameters

One important unknown for the above estimates of planetary deformation is the strength of the elastic lithosphere, which controls the wavelength and magnitude of lithospheric deformation. Although some local analyses of gravity and topography data have constrained lithosphere elastic thicknesses to 10–30 km in a few regions (Genova et al., 2023; Goossens et al., 2022), it is unclear whether these are representative of the entire planet. For example, while small elastic thicknesses on Mars might be adequate to investigate the flexural support of some shield volcanoes (<30 km, e.g., Broquet & Wieczorek, 2019), the support of the broad Tharsis rise requires thicker lithospheres (~60–100 km, Andrews-Hanna et al., 2008; Bouley et al., 2016). The time of loading is also unknown, and this would affect the elastic thickness. Thermal evolution models of Mercury predict the elastic lithosphere to have thickened over time from a few km at the dawn of Mercury's evolution to ~100 km (e.g., Fleury et al., 2024). For these reasons, the elastic thickness of the lithosphere ranges from 10 to 100 km. Higher values have little effect on membrane–flexural strain. We note that although lateral variations in elastic thickness may be expected on Mercury (e.g., Fleury et al., 2024), adequate constraints on the spatial variations in elastic thickness are lacking and solving for elastic deformations with variable shell thickness is not trivial to implement (Beuthe, 2008) and is not accounted for in our model.

Although supported by previous work (e.g., James et al., 2015; Plattner & Johnson, 2021; Tosi et al., 2015), our assumed gradual transition from deep to crustal support of isostatic anomalies (centered at degree 15) does affect the inferred deformation pattern and interior structure. However, this assumption will later be relaxed by leveraging the tectonic record to constrain membrane–flexural deformations (see Section 3.4).

Following previous work, the crust and mantle density are set to 2,800 and 3,200 kg m^{-3}, and the average crustal thickness is set to 30 km (e.g., Genova et al., 2023; Sori, 2018). We note that these parameters have a negligible effect on membrane–flexural strain (<10%) when compared to the elastic thickness of the lithosphere. In addition, we emphasize that lateral variations in crustal thickness are by definition included in our crust and mantle loading models. For the model with mantle support, mantle density variations are assumed to range from the base of the crust down to 400 km depth (see also James et al., 2015). The thickness of the mantle density anomaly directly trades off with the magnitude of the density anomaly and has a small effect on membrane–flexural strains. Young's modulus and Poisson's ratio do affect the magnitude of membrane–flexural strains (with decreasing Young's modulus almost linearly increasing areal strains), but not as strongly as does elastic thickness. This can be simply understood by looking at the flexural rigidity of the lithosphere, which scales as the cube of the elastic thickness and linearly to other parameters. For consistency, these parameters are kept constant and set to 100 GPa and 0.25 following previous work (e.g., Genova et al., 2023).

2.4. Comparison of Membrane–Flexural Strain to Tectonic Strain

In our companion paper (Broquet & Andrews-Hanna, 2026), lateral variations in tectonic strain and shortening were evaluated using global tectonic databases of wrinkle ridges, lobate scarps and high-relief ridges (Klimczak et al., 2025; Watters, 2021) together with a global stereo digital elevation model (Becker et al., 2016). A machine learning algorithm was developed to estimate the heights of shortening landforms (which are hereafter referred to as ridges) and associated displacement variations along each landform. Tectonic strain maps were then constructed by summing the inferred horizontal displacements scaled by the associated ridge segment lengths within a 400-km moving window and dividing by the window area. Additional considerations were implemented to account for overlapping structures and the orientation of features when relating tectonic strain to shortening and contraction, and two tectonic strain models were constructed. Our preferred model uses primary ridges to estimate tectonic strain. Primary ridges are defined as the longest structure along one principal direction in a region, which naturally excludes small scarps on the shoulder of a larger ridge and avoids double counting of the strain from one ridge (see Watters, 2021). In this model, vast regions are predicted to have experienced near-zero contraction and strain ($<0.4 \times 10^{-3}$) compared to other locations with strong tectonic strain concentration ($>10 \times 10^{-3}$; see Figure 1). The second model presented in the companion paper considers all tectonic landforms of the database and generally shows ~20% higher strain and contraction values (see Broquet & Andrews-Hanna, 2026).

The distribution and magnitude of the observed tectonic strain are compared to the modeled strain from loading. For adequate comparisons between the gravity-dependent modeled flexural deformations, the tectonic strain map was re-sampled to the Mercury's gravity field degree-strength in all subsequent analyses. This approach allows the tectonic strain map to preserve high-resolution in the northern hemisphere and be of lower resolution in the south, which is consistent with the resolution of elevation models and associated tectonic strain estimates (e.g., Becker et al., 2016). The wavelength and magnitude of lithosphere deformation from loading are dominantly controlled by the strength of the elastic lithosphere. In order to constrain the elastic thickness in our analyses, we first compare the power spectra of tectonic and membrane–flexural strains. We note that this approach assumes that lateral variations in tectonic strain are, at least partly, due to lithosphere loading. Furthermore, in a power spectrum comparison, positive and negative strains could be reversed while still giving a matching power spectrum. Nevertheless, by focusing only on matching the wavelength of lithosphere deformation, a suitable lithosphere thickness can be identified independent of the other details of the model, such as the compensation mechanism (crustal vs. mantle).

We then compare membrane–flexural and tectonic strain in the spatial domain to evaluate which of our loading models (considering crustal support only or a combination of crustal and mantle support) best fits the tectonic record of strain. Before comparison with the tectonic record, we removed the average global tectonic strain in our tectonic strain map. This highlights regions with a tectonic strain excess and deficit, and provides consistency with the modeled strain, which lacks a degree-0 component. For the spatial comparisons, we compute an area-weighted root-mean-square misfit of membrane–flexural and tectonic strain magnitudes. A strain residual map was also constructed after having removed the contribution of membrane–flexural strain to tectonic strain. The area-weighted standard deviation of this residual map is used to further characterize the best fit elastic thicknesses and loading models.

3. Results

3.1. Constraints on the Elastic Thickness of the Lithosphere

We generated a suite of membrane–flexural areal strain maps as inverted from gravity and topography considering a wide range of parameters. First, to determine the best-fitting elastic thickness of the lithosphere, we performed a power spectrum comparison of tectonics versus membrane–flexural strains. Importantly, and as noted above, the signal is squared in a power spectrum analysis, which in our case discards information on the direction of the principal stresses and the associated type of deformation (compression or extension). While one model might provide a good fit in a power spectrum analysis, it may not necessarily predict the correct stress direction. As the wavelength of deformation is well captured by a power spectrum, such analysis can nevertheless be used to provide first order constraints on the elastic thickness of the lithosphere. The tectonic strain power spectrum results from the degree-strength downsampled tectonic strain map constructed in the companion paper (Broquet & Andrews-Hanna, 2026). Across all degrees, the modeled strains for elastic thicknesses of 60–80 km best match the spectrum of observed tectonic strain, with an elastic thickness of 80 km providing the best match at

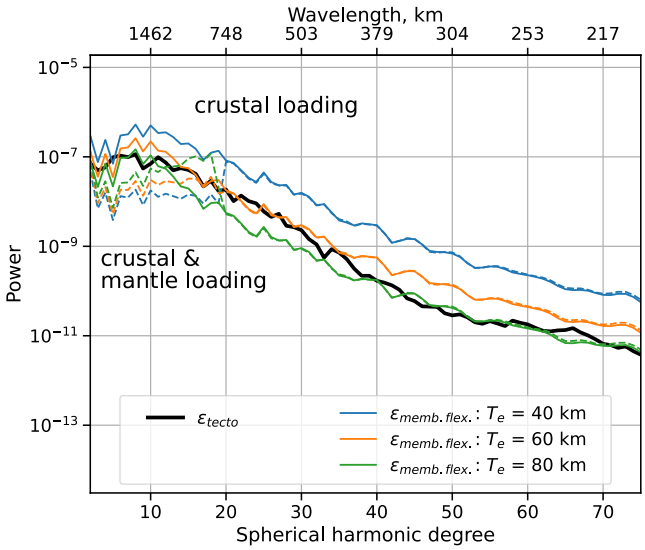

Figure 2. Power spectra of tectonic versus membrane–flexural strain considering different elastic thicknesses for the model assuming crustal loading only (solid) and a combination of crustal and mantle loading (dashed). Both models are equal at degrees >20.

shorter wavelengths (Figure 2). Lateral and time variations in elastic thickness cannot be captured by our loading model and could explain the moderate differences between the observed and modeled power spectra of strain when assuming a globally constant elastic thickness.

In general, the crustal and mantle loading model is seen to predict slightly lower long-wavelength strains, which results from the deep compensation and the additional flexural support coming from the isostatic crust. At shorter wavelengths and per definition in this model, strains are equal to the crustal loading only model. Thus, strains from the combined crustal and mantle loading model are controlled by the assumed transition from isostasy and mantle support to crustal loading at long-wavelengths and by the elastic thickness at shorter wavelengths. Although the model could be tuned to better match the power spectrum of strain, that would not account for real spatial variations in the compensation mechanism in which some areas may be compensated by large-scale mantle density anomalies and others by large-scale crustal loading. Specific regions of interest in the model will be evaluated spatially in the discussion below.

As a complementary approach to evaluate the best input lithosphere elastic thickness, we estimate the area-weighted standard deviation of the difference between the membrane–flexural strain and the tectonic strain map. Both maps have averages of zero as the degree-0 terms have been removed, and thus the average difference between the two must also be 0. The standard deviation of the difference can be used to quantify the spatially varying misfit, and we note that this approach is sensitive to the type of deformation (compression or extension). The loading model associated with the minimum standard deviation best explains the observed heterogeneity in tectonic strain. For both models, we obtain a minimum standard deviation when considering an elastic thickness of 60–80 km with values of ~ 2.0–1.7×10^{-3} and 1.3–1.5×10^{-3}, for the crustal and mantle loading model and for the crust only model, respectively. This standard deviation is lower than when considering an elastic thickness of 40 km ($\sim 2.7 \times 10^{-3}$ and 1.4×10^{-3}) or 100 km ($\sim 2.6 \times 10^{-3}$ and 1.9×10^{-3}). Notably, the lower standard deviation when considering the mantle load indicates that this model provides a better match to Mercury's tectonic record, as further discussed below.

Our evaluation of the power spectra and standard deviations favor elastic thicknesses of 60–80 km, and for simplicity, we will focus here on the 60 km elastic thickness models. Thinner elastic lithospheres lead to higher amplitude and shorter wavelength tectonic strain (models with elastic thicknesses of 40 and 80 km are shown in Figure S2 in Supporting Information S1).

3.2. Membrane–Flexural Strains and Mercury's Interior Structure

The areal flexural strain for both the crustal loading and the crustal and mantle loading models considering our preferred elastic thickness of 60 km are shown in Figure 3. Throughout the paper, we will focus on regions located in the northern hemisphere, as the gravity field is better resolved there. The model with crustal loading only predicts prominent compression within the Caloris basin, the Du Fu region, Otaared Planitia, as well as in the northern and Budh-Sobkou rises, and extension over most of the northern smooth plains (Figures 3a–3c). Predicted strains are generally higher in the northern hemisphere reaching values of 5×10^{-3}. Given the long-wavelength signature of our inferred strain highs, this pattern is unlikely to stem only from the uneven resolution of the MESSENGER gravity field models.

The model with long-wavelength deep mantle support also uses a nominal elastic thickness of 60 km (see also Figure S2 in Supporting Information S1). This loading scenario predicts long wavelength strain patterns that are the opposite of the crustal loading model (Figures 3d–3f). Therein, zones with gravity anomaly highs, such as the Caloris basin, the Budh-Sobkou or northern rises, are supported by low-density mantle anomalies (see also James et al., 2015) leading to predicted uplift and extension. On the other hand, negative gravity anomalies are related to high-density mantle anomalies and crustal compression, such as in the northern smooth plains. As noted above, membrane–flexural strains are slightly lower, $\sim 3.0 \times 10^{-3}$ than in the crustal loading model, due to the deep mantle loading and isostatic crust supporting part of the lithospheric loads.

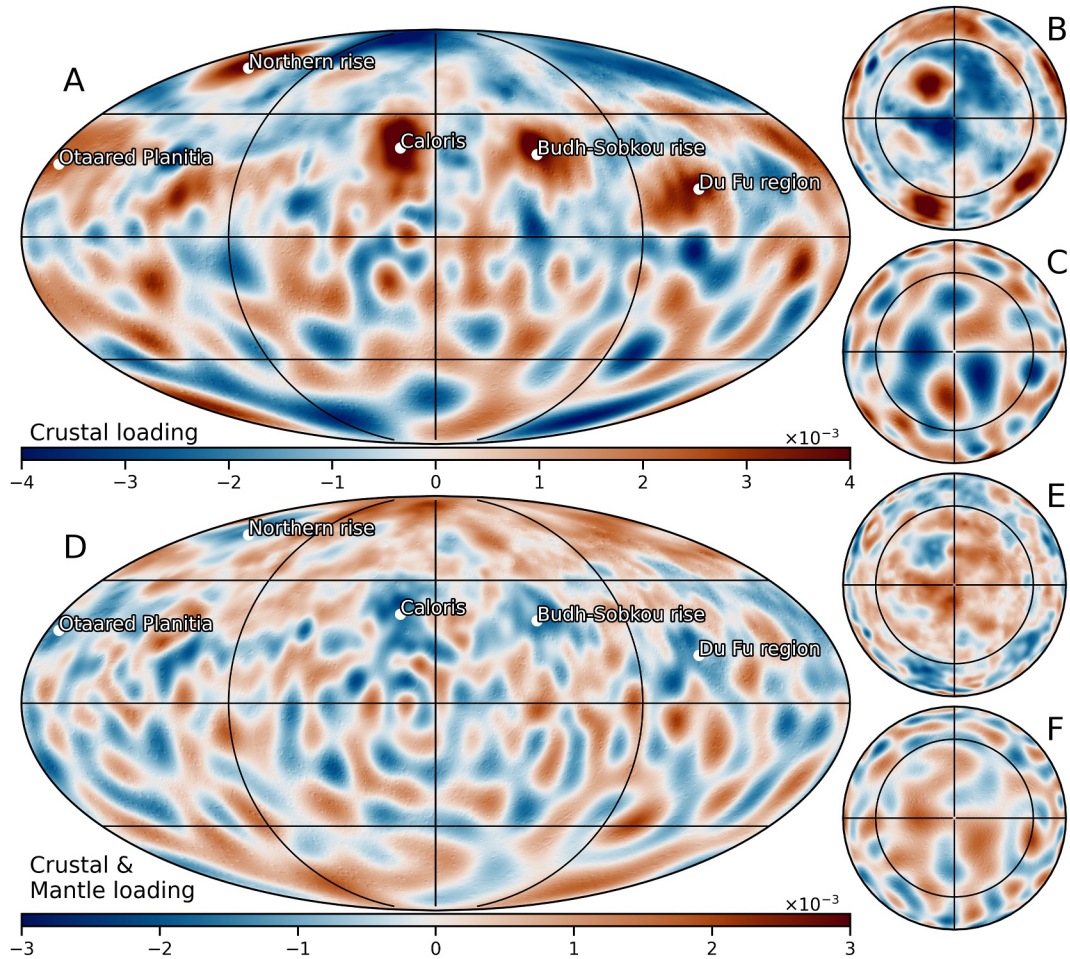

Figure 3. Mollweide projection (left) with north and south polar (top right, bottom right) projections of areal membrane–flexural strain from gravity and topography assuming crustal loading only (a–c) and both crustal and mantle loading (d–f). Compression is positive. Note the difference in strain magnitudes between the top and bottom plots.

The inferred crustal thickness associated with both loading models shows comparable variations (Figures 4a and 4c) with thick crusts just outside the northern volcanic province and thin crusts in the Caloris basins and beneath the Budh-Sobkou and the northern rises. The thinner crust beneath these rises could be a result of the crustal stretching and thinning expected in areas of dynamic uplift, as also seen at Hesperia Planum on Mars (Broquet & Andrews-Hanna, 2023b). We note that our crustal thickness maps do not depend on the assumed elastic thickness and are generally consistent with previous work (see Beuthe et al., 2020; Broquet et al., 2025; James et al., 2015).

Interestingly, mantle density variations obtained by the combined crust and mantle loading inversion appear to follow Mercury's long-wavelength surface temperature pattern with positive density anomalies (colder mantle) at the cold poles along the equator and negative anomalies (warmer mantle) at the hot poles (Figures 4b and 4d). This inversion result is in agreement with theoretical predictions suggesting that Mercury's long-wavelength gravity and topography are related to the planet's surface insolation pattern (Tosi et al., 2015). Alternatively, this apparent pattern could also be the result of the expression of the rotational-tidal distortion of Mercury in the mantle density anomaly model. As both effects are known to exist, a combination of the two is likely. We note that the magnitude of density anomalies trades off with the depth over which they are assumed to occur in our model, and that larger magnitude anomalies confined to shallower depths would also fit the data. We note that density anomalies could also be due to variations in mantle composition, particularly at intermediate wavelengths, between spherical harmonic degrees 3 and 15, as further discussed below.

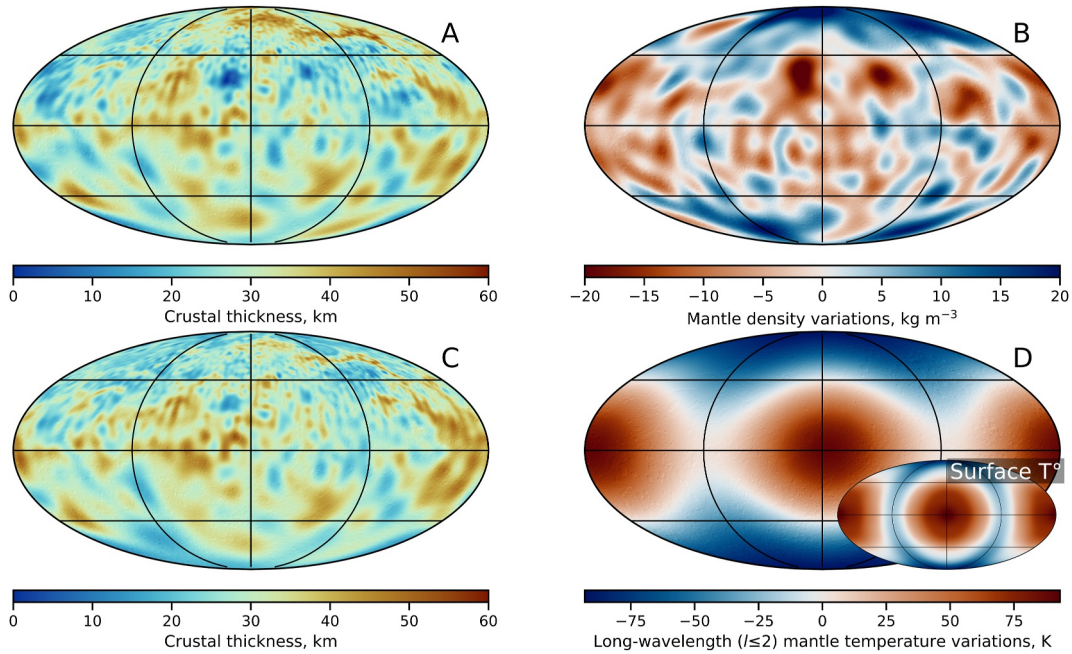

Figure 4. Crustal thickness (a) and mantle density variations (b) as predicted by the mantle support and isostatic crust model. Crustal thickness for the crustal loading model only (c). Mercury's predicted degree-1 and -2 mantle temperature variations (assuming a thermal expansivity of 3×10^{-5} K^{-1} and a mantle density of 3,200 kg m^{-3}) by the mantle support and isostatic crust model (d) compared to the present-day surface temperature pattern (bottom right inset of panel (d)).

3.3. Comparison to the Strain Distribution

Below, we compare membrane–flexural strains to our preferred tectonic strain map constructed using primary landforms. A similar analysis using an alternative tectonic map constructed using all tectonic landforms is also discussed and is shown in the Supplementary Table. As discussed above, we have removed the average global tectonic strain from our tectonic strain map to highlight regions with a tectonic strain excess and deficit. This also provides consistency with the modeled strain, which lacks a degree-0 component. In these maps, areas with less compression than average have negative values, but still experienced net contractional strain.

The crustal loading model displays membrane–flexural strains that are consistent with the tectonic strain excess observed in many regions of the southern hemisphere (Figures 5a and 5c). In these regions, membrane–flexural strain from crustal loading contributes to a large fraction, if not all, of contractional tectonic strain. A correlation between a tectonic strain deficit and modeled extensional strains in the northern smooth plain regions is also observed, and indicates that regional membrane–flexural strain can counteract contractional strain as well as add to it. However, the tectonic strain excess in some lobate scarp covered regions of the southern hemisphere cannot be explained by crustal loading alone, though membrane–flexural strains are affected by the low resolution of the gravity data. Notably, the crustal loading model predicts contractional strain concentrations in the Caloris basin and the Otaared, Budh-Sobkou, and Du Fu regions, which is opposite to the deficit observed in the tectonic record.

By design, the flexural model with mantle support predicts strains that are opposite to the crustal loading model at long wavelengths, and is generally more consistent with our tectonic strain map. Although membrane–flexural strains have lower magnitude in the case of mantle support when compared to crustal loading, the predicted extension helps to explain the strain deficit in the Otaared Planitia, Northern rise, Du Fu and Budh-Sobkou regions (Figures 5b and 5c). This indicates that uplift in these regions must either pre-date (with remnant extensional strain in the lithosphere counteracting some of the later contraction) or have happened concurrently to the major phases of Mercury's global contraction. Predicted uplift at the Caloris basin for this model is also consistent with the general tectonic strain deficit as well as with the many extensional tectonic landforms that have been observed in the crater floor (see also, Freed et al., 2009). In the northern smooth plains and in the southern hemisphere, the mantle support model predicts prominent positive mantle loads inducing crustal compression. Although this

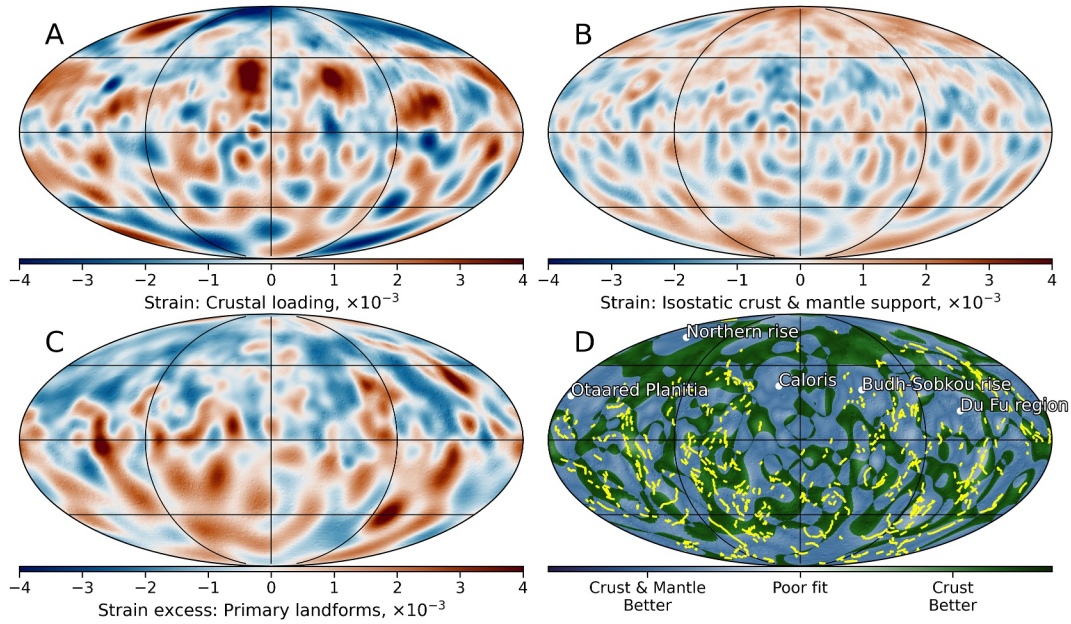

Figure 5. Comparison of tectonic and membrane–flexural strains. Membrane–flexural strain for crustal loading only (a) and with an isostatic crust and mantle support at long wavelengths (b) as compared to tectonic strain excess (c). Misfit of tectonic strain versus membrane–flexural strains (d). Dark green colors indicate a better fit of the crustal model, while dark blue colors show a better fit for the crustal and mantle support models. Light colors indicate a poor fit with no preference for either model. Some regions are annotated for context and yellow lines in (d) show high-relief ridges and lobate scarps mapped in Watters (2021). Note that the strain excess map in (c) has been downsampled to match the gravity field resolution in the southern hemisphere.

flexural compression would contribute to the regional strain, completely neglecting the compressional tectonics in this region would underestimate the contractional strain.

To identify the model that best fits the tectonic record, we performed a spatially dependent misfit between the magnitude of membrane–flexural and tectonic strains, corrected for global contractional strain. If the laterally variable tectonic strain were solely due to membrane–flexural deformations, these deformations would fully correct for tectonic strain excesses and deficits and the misfit would be exactly zero. For each location on the surface, we quantify whether the crust-only or crust–mantle loading model provides a better fit to the observed tectonic strain and retains the minimum misfit for either model (Figure 5d). Based on this misfit comparison, we observe the model with mantle support to provide a better fit to our preferred primary tectonic strain excess and deficit over 60% of Mercury's surface and thus is the preferred model. Importantly, we note that neither loading model is able to fully explain the magnitudes of the tectonic strain excesses and deficits, and an alternate model is discussed in Section 3.4. When using the other tectonic strain map, which uses all tectonic landforms and is generally not preferred (Broquet & Andrews-Hanna, 2026), the mantle support model is also seen to provide a better correction over 60% of Mercury's surface (Figure S3 in Supporting Information S1). However, some differences are observed in the northern hemisphere, including the northern rise and the Caloris basin turning into tectonic strain excess, which we attribute to the double-counting of ridges associated with multiple closely spaced faults. The tectonic strain deficit in the Budh-Sobkou rise, Du Fu region and Otaared Planitia persist and remain consistent with the mantle support model, implying that these observations are robust and independent from the details of the tectonic mapping.

For the elastic thickness analysis, we also estimated the area-weighted standard deviation of the membrane–flexural strain corrected tectonic strain map. For the crustal loading model only, we obtain a standard deviation of $\sim 2.0 \times 10^{-3}$, which is about 50% higher than when using the combined mantle and crust loading model for which the standard deviation is 1.3×10^{-3}. This again confirms that the combined model provides a better explanation for the observed tectonic strain excesses and deficits.

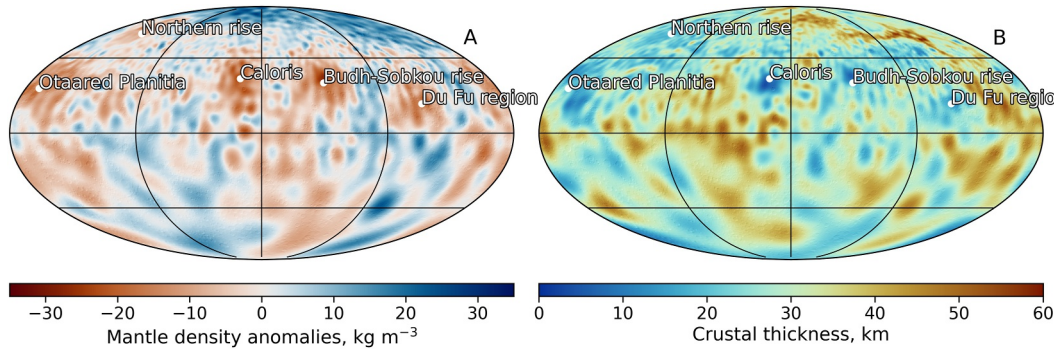

Figure 6. Mantle density anomalies (a) and crustal thickness (b) as inverted from gravity, topography, and tectonic deformations.

3.4. A Gravity and Topography Inversion Constrained by Tectonic Deformations

In previous sections, our inversion for lithosphere deformation and interior structure that necessitates three inputs was constrained using observed gravity and topography and by assuming the type of loading (i.e., crustal or mantle). Alternatively, it is possible to construct an inversion of gravity and topography under the assumption that membrane–flexural strains are equal to tectonic strains. Local tectonic strain excess is interpreted as being due to membrane–flexural subsidence, whereas strain deficits are converted to membrane–flexural uplift. The degree-strength downsampled tectonic strain map is converted to membrane–flexural uplift and subsidence using a spectral transfer function similar to an admittance. This transfer function was constructed using the spectral ratio of membrane–flexural deformation and strain, as predicted by our nominal gravity and topography inversions. Although strain is related to the second derivative of the displacement, strictly speaking, areas of uplift are generally associated with extensional strain and subsidence with contractional strain. By using tectonic strain as a simplified proxy for displacement, the problem becomes linear and is easily solved by our model.

In this novel inversion approach, the loading type is self-consistently determined based on the observed deformations (no loading type needs to be input), but lateral variations in the observed tectonic deformations are assumed to be fully due to membrane–flexural strains. Effectively, this model uses the tectonic strain to constrain the relative importance of mantle and crustal loading as a function of spherical harmonic degree, rather than the imposed ratio in the hybrid crust-mantle loading model shown above. In this model, membrane–flexural deformations better correct the observed regional tectonic strain excesses or deficits (Figure S4 in Supporting Information S1), leading to a misfit standard deviation of 0.5×10^{-3}, which is substantially lower than for the crust–mantle (1.3×10^{-3}) or crust-only (2.0×10^{-3}) loading models. The misfit is dominated by a degree-1 signal that is typically not well estimated by thin-shell models and excluding this degree-1 offset leads to a misfit standard deviation of only $\sim 0.25 \times 10^{-3}$. The improved agreement between the model predictions and observed strain justified the assumed use of tectonic strain as a proxy for lithospheric displacement.

As with the combined crustal and mantle support model, the inversion predicts the presence of a broad low-density mantle supporting the Otaared Planitia, Northern rise, Budh-Sobkou rise, Caloris basin, and the Du Fu region (Figure 6a). Note that because this model doesn't limit the mantle support to a specific wavelength, some shorter-wavelength and higher amplitude mantle density anomalies are predicted when compared to our previous combined loading model (Figure 4b). A large-scale positive mantle density anomaly (possibly a cold downwelling) is predicted over the northern smooth plains, leading to subsidence and contractional strains. A prominent positive density anomaly and downwelling was also observed in the south-east and near the Astrolabe Rupes region (near 45°S 80°W). For this model, crustal thickness is consistent with previous inversions, displaying generally thinner crusts over a low-density mantle, as it is primarily constrained by gravity and topography and the assumed crust and mantle densities and less affected by mantle density anomalies (Figure 6b). This inversion further demonstrates that long-wavelength support of topography by mantle density anomalies is an important factor to consider when investigating regional tectonics on Mercury.

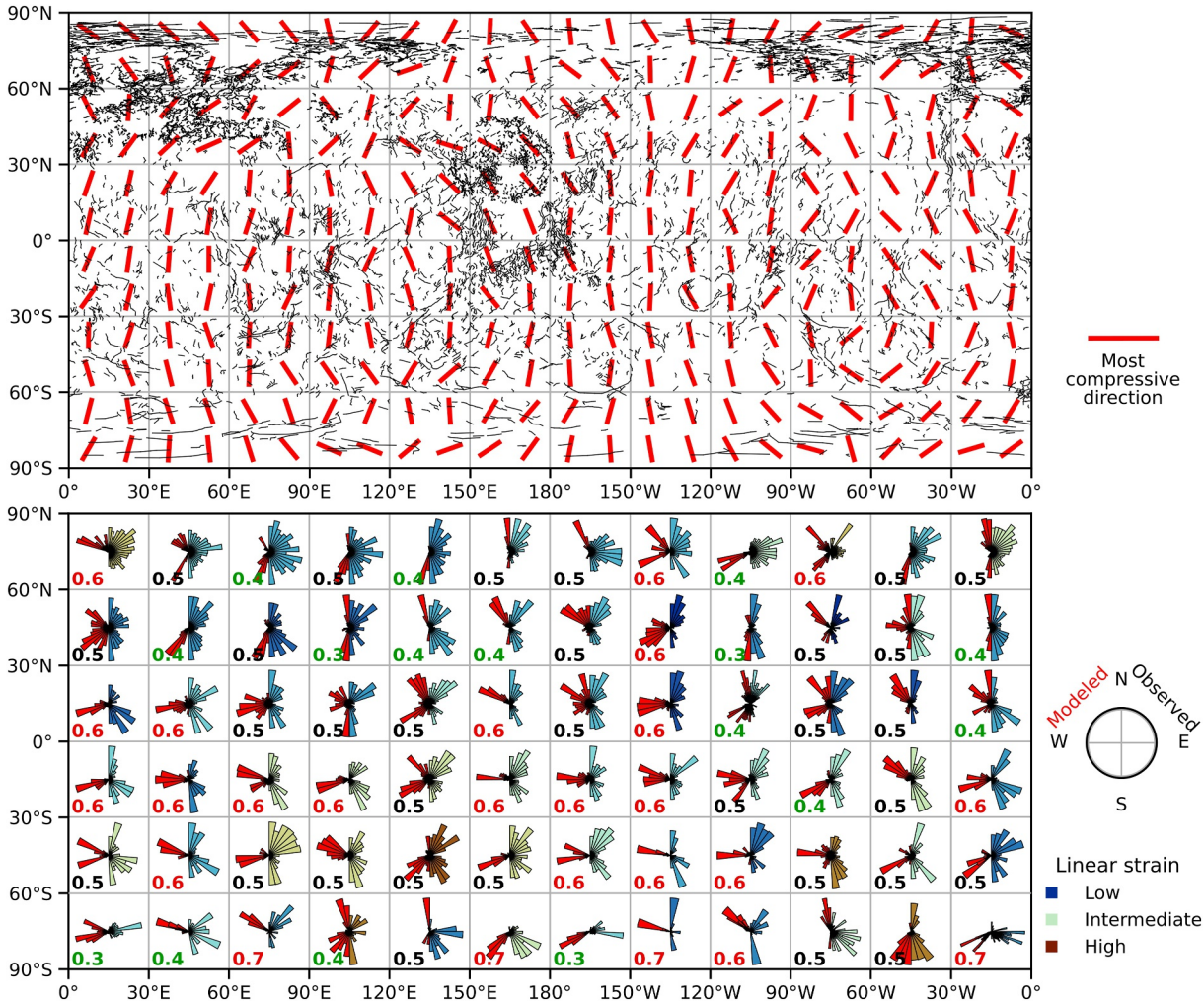

Figure 7. Comparison of the direction of tectonic landforms and the most compressive membrane–flexural stresses for our preferred model. Tectonic landforms as mapped by Klimczak et al. (2025) together with the predicted most compressive stress orientation within 7.5° bin (top). Observed (colored; right side) and predicted (black; left side) direction at each landform location per 30° × 30° quadrant in rose diagrams (bottom). The color-code indicates the linear strain. A symmetrical normalized color-coded misfit value is given in the bottom right corner of each sector (0: aligned, 1: orthogonal).

As this approach provides a much-improved fit to the observed tectonic strain and does not require assumptions on how crustal and mantle loads are partitioned, this model is preferred over the two inversions discussed above. Below, we provide further analyses on the membrane–flexural strains associated with this preferred model.

3.5. Effect of Membrane–Flexural Deformations on the Orientation of Tectonic Landforms

Mercury's global tectonic fabric displays a non-random orientation. To estimate how membrane–flexural strains affect the tectonic expression of global contraction, we performed a rose diagram analysis similar to Klimczak et al. (2025). The planet is subdivided into multiple 30° × 30° sectors and the observed direction of faulting (normalized to 0–180°) is compared to the principal direction of the most compressional stress from our modeled membrane–flexural stress tensor using our preferred model discussed in the above section (Figure 7). This approach averages out variations in strain orientation at scales smaller than we can resolve in the gravity data, focusing instead on regional patterns. For each sector, we provide a linear-strain-weighted rose diagram indicating both the observed and modeled directions of faulting. We consider that a fault orientation is consistent with membrane–flexural compression if the predicted direction of faulting (i.e., the perpendicular to the most compressive direction) is aligned with observations. A symmetrical normalized misfit value is also given for each sector, with low values indicating alignment between our model predictions and observations, and reaching

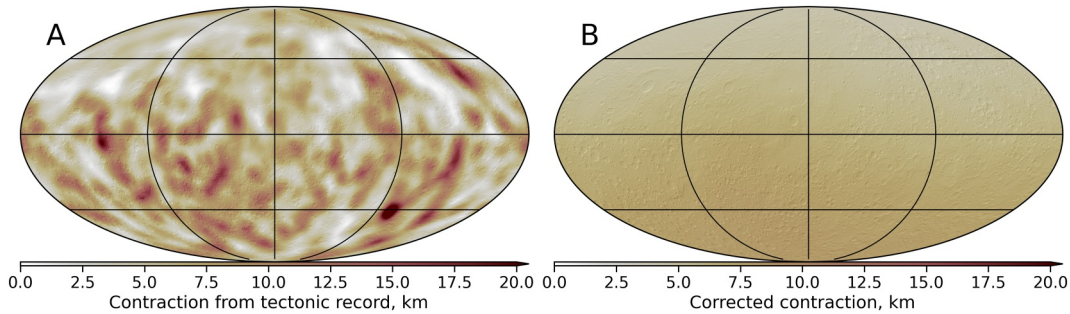

Figure 8. Global contraction as predicted from the tectonic record (a) and corrected for membrane–flexural strains using the model developed in Section 3.4 that uses tectonic strain as a proxy for membrane–flexural deformations (b).

values of 1 for orthogonal and inconsistent predictions. A misfit value of <0.5 indicates that membrane–flexural deformation has likely significantly affected the orientation of tectonic landforms. For regions with a higher misfit value, the direction of faulting was controlled using other processes.

The area- and tectonic-strain weighted average symmetrical normalized misfit is ∼0.52, which shows that our inferred principal direction does not significantly affect the orientation of observed landforms. Thus, although membrane–flexural strain can account for Mercury's tectonic strain excess and deficit, some other processes control the direction of faulting. In particular, it has been suggested that the north-south orientation of lobate scarps near the equator results from planetary despinning (Klimczak et al., 2015; Matsuyama & Nimmo, 2009). Some other faults display preferred orientations with respect to the Caloris basin and other large basins that may have created zones of crustal weakness (e.g., Klimczak et al., 2025). The lithosphere can also inherit a fabric from previous episodes of tectonism that have been buried or erased. This fabric will affect the direction of faulting, as it is often easier to reactivate an existing fault than to create a new one (e.g., Dombard & Hauck, 2008). Most of these processes cannot be captured by our inversion of strains and associated prediction of the direction of faulting. If the magnitude of strains from global contraction greatly exceeds the magnitude of the membrane-flexural strains, then fault patterns will initially be random and strain release in both horizontal directions will be required, which may also contribute to the high misfit. Large magnitude contractional strain will require release of strain in the direction orthogonal to the membrane-flexural compression, which can lead to a pattern of orthogonal sets of faults (as found in some areas) or to the development of disorganized faulting after the release of the dominant membrane-flexural strain (as particularly observed in regions covered by wrinkle ridges). This process likely contributes to the apparent poor correlation between the predicted and observed directions of faulting.

4. Discussion

4.1. Mercury's Radial Contraction Corrected for Membrane–Flexural Deformations

Mercury's tectonic record is largely heterogeneous, with some regions having preserved important compressional deformations compared to others devoid of shortening landforms. In the sections above, we argue that Mercury's tectonic fabric has been prominently influenced by local lithospheric deformations unrelated to global cooling. Here, we use membrane–flexural to shed light on how regional lithospheric loading might have affected Mercury's tectonic record and the accumulated global contractional strain.

We use our preferred membrane–flexural strain model described in Section 3.4, in which uplift and subsidence are inferred from observed tectonic deformations. When used together with observed gravity and topography, this inversion self-consistently determines the interior loads without assuming how crustal and mantle loads are partitioned. Importantly, we note that this model assumes that Mercury's heterogeneous tectonic record can be explained by membrane–flexural deformations and present-day gravity and topography data. This approach also neglects the possible contribution of lateral variations in crustal strength and cooling rate. Nevertheless, this model is able to nearly fully correct for Mercury's heterogeneous record of tectonic strain, while being fully consistent with the observed gravity and topography (Figure 8). As our model corrects for both tectonic strain excesses and deficits, this correction has no effect on the global average contraction. Thus, we conclude that

future work must consider membrane–flexural strain as an important contribution to Mercury's regional tectonic records, which can both increase and decrease the local strain.

4.2. Mantle-Induced Uplift

One potentially important contribution to the tectonic record is deformation that has not been preserved in the present-day planetary gravity and topography. Geological and geophysical observations suggest that Mercury's long-wavelength topography has changed after the major basin-forming epoch, resulting in long-wavelength rises such as the Budh-Sobkou (Zuber et al., 2012). Our analyses support the interpretation that these long-wavelength rises are due to mantle density anomalies, as suggested in a previous work (James et al., 2015). It is also possible that similar deformation could have occurred in the past and not be expressed in the present-day gravity and topography, as might occur from the transient effects of a mantle plume. This transient deformation could be expressed in the tectonic record, but not in the gravity and topography, leading to some biases in our inferred interior structure of Mercury. The Hesperia Planum volcanic province on Mars is a good example (Broquet & Andrews-Hanna, 2023b). Hesperia Planum is covered by wrinkle ridges with a tectonic strain that is substantially higher than on similarly aged surfaces and in the surroundings, which indicates that an important loading event affected the tectonic record. However, the present-day regional gravity and topography do not indicate the presence of a substantial load currently acting on the lithosphere. To explain this discrepancy, Broquet and Andrews-Hanna (2023b) proposed a loading sequence of plume-induced uplift, volcanism, and subsidence, following an evolutionary path similar to flood basalt provinces on Earth. In that framework, the Hesperia Planum flood basalt formed under stress-free conditions on an uplifted surface. As the plume-induced uplift subsided down, flood lava recorded important contractional strains. Because the surface went back to its initial state after the thermal deflation of the plume head, both the regional gravity and topography are not expected to preserve appreciable signatures of the dynamic process that occurred.

Some regions in Mercury's southern hemisphere show a local tectonic strain excess that is not explained by our crust and crust–mantle loading models (Figure 5), and a similar geodynamic history could help explain their tectonic record. As in Hesperia Planum, these areas, including in the Astrolabe or Discovery Rupes region (near 45°S 80°W), sit in a relative depression when compared to the surrounding terrains, which could be the relics of a geodynamic sequence involving a mantle plume if the plume was associated with volcanic outpourings. Alternatively, a past downwelling of dense material could cause local compression that would persist after the downwelling density anomaly had dissipated. However, the poor resolution of the gravity field in the southern hemisphere could hide the signatures of present-day mantle density anomalies.

Importantly, unlike Hesperia Planum, the density anomalies below the rises were likely present before or during the major phases of planetary contraction (>3 Ga), and must be still present today in order to express their signature in observed gravity and topography data. Such long-lived density anomalies are not compatible with simple thermal plumes of hot material arising from the core-mantle boundary (e.g., Campbell, 2007), which although stable early in Mercury's geologic history are not typically maintained after 3 Ga (Jain & Solomatov, 2024; Tosi et al., 2025). We thus argue for the presence of a persistent compositional density anomaly. Importantly, we also note the non-negligible contribution of temperature anomalies associated with the planet's 3:2 spin–orbit resonance, the effect of which is thought to propagate all the way through the mantle (Tosi et al., 2015). Such a long-wavelength pattern is consistent with the position of the major rises in the northern hemisphere and could thus also contribute to their dynamic support.

4.3. Surface and Interior Temperature Changes

Thermal evolution models indicate that a substantial fraction of Mercury's degree-2 and 4 topography and geoid could be dynamically supported by mantle density anomalies related to the planet's peculiar surface temperature pattern (Tosi et al., 2015). Our membrane–flexural strain inversion with mantle support also predicts that long-wavelength mantle density anomalies are correlated with surface temperature (Figure 4d). Mercury's present-day surface temperature ranges from about 230 to 460 K (Vasavada et al., 1999). If this pattern varied over geologic time, due to the orbital evolution of the planet, including spin–orbit resonance switches (Wieczorek et al., 2012) or true polar wander, this could lead to regional cooling rates greater than expected from radioactive decay and interior cooling of about 25 K/Gyr (Hauck et al., 2004; Tosi et al., 2013). Thus, changes in Mercury's orbital history and associated surface temperature could have substantially affected the planet's tectonic history.

Given the important lateral variation in surface temperature on Mercury, the yield strength of the lithosphere is expected to also vary spatially. The viscous portion of the lithospheric strength envelope is strongly temperature-dependent and zones with higher surface temperature would have thinner and weaker lithospheres. These regions would have faulted more readily and displayed greater tectonic strains (e.g., Tosi et al., 2025; Williams et al., 2011). Regions with thinner elastic lithospheres would also record more membrane–flexural strains, as discussed in the above section, which could either amplify or diminish this effect.

Planetary cooling is dominated by radioactive decay, which in turn depends on the concentration of heat-producing elements in the crust and mantle. Data from the MESSENGER Gamma-Ray Spectrometer indicate substantial and up to 10-fold variations in the surface concentration of both K and Th (Peplowski et al., 2012), though how this relates to their abundances at depth is unknown. This substantial uncertainty in the average concentration of heat producing elements in the crust and mantle and the spatial variations thereof leads to considerable uncertainty in available estimates of planetary cooling and contraction. In addition, uncertainties in the core structure, including the size of the inner core, together with the amount of core crystallization and timing of inner core growth all have important effects on Mercury's contraction history (e.g., Davies et al., 2024).

4.4. The Hidden or Lost Record of Contraction

Even after yielding, materials can preserve a non-negligible amount of strain in their frictional yield strength (e.g., Byerlee, 1978). As discussed in Klimczak (2015) and in our companion paper (Broquet & Andrews-Hanna, 2026), some kilometers of global contraction could be accommodated in the lithosphere's frictional strength. Horizontal compression can also be accommodated by lateral compaction of the pore space in the ancient crust (Andrews-Hanna & Broquet, 2023). Although Mercury's crustal porosity is mostly unknown, it is expected to range from 9% to 18% based on the crater and basin population (Broquet et al., 2024). Lateral compaction of 1% porosity can accommodate a strain of 1% (equivalent to a radius change of 2.4 km). Thus, pore compaction could have contributed substantially to the non-tectonic accommodation of planetary contraction.

As previously suggested for Mars (Andrews-Hanna & Broquet, 2023), part of Mercury's tectonic strain could also be expressed in the form of small-scale ridges that are below the resolution of the fault database of Klimczak et al. (2025). The artificial smoothing of elevation data produced during the construction of the global DEM also leads to an underestimation of the heights of the tectonic landform, ultimately leading to an underestimation of global contraction. The laser altimeter and high-resolution imaging cameras onboard the incoming BepiColombo mission (Thomas et al., 2021) would help better map Mercury's surface globally and determine the contribution of small-scale tectonic landforms to planetary contraction estimates.

A non-negligible fraction of tectonic landforms on Mercury might have been erased or covered using geologic processes. Any landform dating to early in the planet's history might not have been preserved, being either destroyed by impacts or resurfaced by volcanic events. The relatively young age of Mercury's upper crust (~4.1 Ga) implies that about 10% of the planet's contraction and tectonic history have been lost by resurfacing events, depending on the time history of cooling and contraction.

Although smooth plains are thought to be relatively thin (e.g., Du et al., 2020; Ostrach et al., 2015), the apparent lack of high-relief ridges and lobate scarps in smooth plain covered regions suggest their burial or possible erasure by volcanic flows. Interestingly, a similar erasure of topographic scarps by flood volcanism has been suggested on the Moon. While Mare Imbrium's kilometers-high and tens of km wide middle and outer rings are clearly expressed in the eastern part of the basin, a western ring is completely absent (Broquet & Andrews-Hanna, 2024; Liang et al., 2023). Mare-induced thermo-mechanical erosion could have led to the erasure of this ring system. Similarly, smooth plain volcanism could have erased or simply buried a substantial part of Mercury's tectonic record in a large fraction of the planet's surface. The poor resolution of Mercury's gravity field models, however, impedes the investigation of buried tectonic structures.

Burial of existing compressional landforms could partially account for the strain deficit observed in the smooth plain covered Otaared region. However, our work indicates that other smooth plains have recorded a compressional tectonic strain similar to the cratered terrain (Broquet & Andrews-Hanna, 2026). Together with the relatively early formation age of smooth plains (~3.7 Ga; e.g., Wang et al., 2021) and the expected subsequent global contraction of Mercury (e.g., Tosi et al., 2013), some other processes must have affected Otaared Planitia, including membrane–flexural uplift, as discussed in this work.

5. Conclusion

In this work, present-day gravity and topography data were inverted for Mercury's interior structure and associated deformation of the lithosphere. Two compensation scenarios were explored, including crustal loading only and a combination of crustal loading and long-wavelength support of topography from the mantle (see also James et al., 2015; Watters et al., 2021). Similar to previous work, we find that Mercury's long-wavelength topography and gravity can be explained at least in part by mantle density anomalies connected to the planet's 3:2 resonance and degree-2 surface temperature pattern (Tosi et al., 2015). The membrane–flexural strains predicted from these models show magnitudes that are comparable to the tectonic record and can partially explain Mercury's uneven tectonic fabric.

On a global scale, we use the combined mantle and crustal loading model to better explain the observed uneven distribution of shortening landforms and their associated contractional strain deficits and excesses. At a local scale, strains inferred from the tectonic record exhibit prominent lateral variation, with some regions experiencing near-zero strain, while others recorded strains up to 10×10^{-3}. In particular, there is a general deficit in compressional tectonics in the northern and Budh-Sobkou rises as well as the Caloris basin, the Otaared, and Du Fu regions, all of which are located in the northern hemisphere of Mercury. While some regions in the southern hemisphere also display a heterogeneous tectonic record, the low resolution of gravity data in that hemisphere hinders accurate interpretations. Our loading model with long-wavelength mantle support systematically predicts uplift and extension in the aforementioned regions of the northern hemisphere, thereby providing an explanation for the local tectonic strain deficit (see also Watters et al., 2021). This indicates that flexural uplift at these regions must either pre-date or have occurred concurrently to global contraction, early in Mercury's geologic history.

Tilted crater floors in some areas of the northern hemisphere are consistent with mantle support of the topography that post-dates Mercury's resurfacing event near 4.0–4.1 Ga (Balcerski et al., 2013; Zuber et al., 2012), and implies tectonic contraction at times <4.1 Ga. The constraints on the long-wavelength deformation from tilted craters and tectonics limit the period in which these mantle density anomalies were established to a relatively narrow window early in Mercury's history. Similarly, our analysis of the tectonic record of Mercury indicates that contractional strain rates were much higher earlier in the planet's history (~4.0–4.1 Ga; Broquet & Andrews-Hanna, 2026). These results indicate that long-wavelength support of topography from mantle density anomalies was established early and stable during a substantial fraction of Mercury's contraction history. Ancient fossilized uplift, preserved as the lithosphere thickened, could also contribute to the observed strain deficit at the major rises. However, our model demonstrates that an additional load, expressed as a low-density anomaly in the mantle, is required to fit Mercury's gravity field. This observation is more consistent with a stable and ongoing support of the topography. In addition, if the fossilized uplift were due to ancient thermal anomalies, the anomalies would have cooled as the lithosphere thickened and the surface would have likely returned to its original undeformed state (e.g., Broquet & Andrews-Hanna, 2023a, 2023b).

Mercury's interior is most likely not convecting at present-day (e.g., Jain & Solomatov, 2024), and thus long-lasting compositional anomalies might be a more likely explanation for the mantle density variations than thermal anomalies. As an example, and given the planet's relatively small mantle and observed magmatic history (e.g., Beuthe et al., 2020; Weider et al., 2012), spatial variations in melt extraction might have created prominent compositional mantle anomalies (i.e., a more primitive vs. depleted mantle). In the absence of convection, such anomalies could be stable and be preserved over long-timescales, thereby explaining our inferred mantle density variations and their effect on Mercury's long-term contraction history.

Although we here argue for long-standing compositional mantle density anomalies supporting the topography, deflection of the core-mantle boundary (James et al., 2015) or some level of crustal underplating (Phillips et al., 1990) may also contribute. The presence of a deep-seated magnetic anomaly, close to the core-mantle boundary, associated with the northern rise supports a deep origin of gravity anomalies (Plattner & Johnson, 2021).

Other regions with a tectonic strain excess or deficit can also be partly explained by local lithospheric deformation, and this indicates that membrane–flexural strains can counteract contractional strain as well as add to it. In the northern smooth plains, the mantle support model predicts prominent membrane–flexural compression. Although such compression would partially contribute to the overconcentration of wrinkle ridges and the

associated regional strain, completely neglecting the compressional tectonics in this region would underestimate the contractional strain, as globally mantle support both adds to and counteracts contractional strain.

We have further developed a novel inversion approach that uses tectonic strain to predict membrane–flexural deformation. When used in combination with observed gravity and topography data, it is possible to self-consistently model Mercury's interior mass distribution. This model also predicts the presence of substantial density anomalies in the mantle, connected to the northern and Budh-Sobkou rises as well as the Caloris basin, the Otaared, and Du Fu regions, thereby supporting our conclusions. As this approach provides a much-improved fit to the observed tectonic strain and does not require assumptions on the compensation mechanism, this model is preferred over the two inversions discussed above. For this model the predicted membrane–flexural strains are nearly identical to tectonic strain (per model definition), and this indicates that local lithospheric deformation can largely explain Mercury's heterogeneous tectonic record.

Although our inversions can match the magnitude and distribution of tectonic strain, our predicted directions of faulting were found to be inconsistent with observations. This disagreement demonstrates that other factors, such as impact-induced zones of weakness (e.g., Klimczak et al., 2025), exert a prominent control on the orientation of tectonic landforms. The disagreement can also be explained if the total magnitude of contractional strain is much greater than the superposed membrane-flexural strains, such that the latter do not exert a strong control on the fault distribution and faults orthogonal to both horizontal principal strain directions are allowed. Further analyses of such correlations could help to place crucial constraints on the timing of global contraction relative to the large basin formation period.

Importantly, as membrane–flexural deformations both increase and decrease the local strain, they have no net effect on the global contraction estimate. Therefore, our global average contraction estimate of 6.3 km remains unchanged (Broquet & Andrews-Hanna, 2026). Nevertheless, future work must consider membrane–flexural strains as an important contribution to Mercury's tectonic record, which can increase and/or decrease the local strain.

Conflict of Interest

The authors declare no conflicts of interest relevant to this study.

Availability Statement

Mercury's global DEM is available at the USGS Astrogeology website (https://astrogeology.usgs.gov/) and the tectonic map is available at Klimczak et al. (2024). The tectonic catalog containing ridge height, together with our membrane–flexural and tectonic strain maps, as well as our crustal thickness and mantle density models, can be found at Broquet (2025). The gravity model used in that work is from Genova et al. (2023) and the membrane–flexural strain code is available at Broquet (2024).

Acknowledgments
This work was supported by a Alexander von Humboldt grant and an Emmy Noether Junior Group Leader grant from the DFG to AB, as well as by NASA Grant 80NSSC22K1340 to JCAH. We thank two anonymous reviewers for their comments that helped improve our manuscript, and Nicola Tosi for stimulating discussion regarding Mercury's contraction history. Open access funding enabled and organized by Projekt DEAL.

References

Andrews-Hanna, J. C., & Broquet, A. (2023). The history of global strain and geodynamics on Mars. *Icarus*, *395*, 115476. https://doi.org/10.1016/j.icarus.2023.115476

Andrews-Hanna, J. C., Zuber, M. T., & Hauck II, S. A. (2008). Strike-slip faults on Mars: Observations and implications for global tectonics and geodynamics. *Journal of Geophysical Research*, *113*(E8), E08002. https://doi.org/10.1029/2007JE002980

Balcerski, J. A., Hauck, S. A., Sun, P., Klimczak, C., Byrne, P. K., Phillips, R. J., & Solomon, S. C. (2013). New constraints on timing and mechanisms of regional tectonism from Mercury's tilted craters. In *44th Lunar and Planetary Science Conference* (p. 2444).

Banerdt, W. B. (1986). Support of long-wavelength loads on Venus and implications for internal structure. *Journal of Geophysical Research*, *91*(B1), 403–419. https://doi.org/10.1029/JB091iB01p00403

Becker, K. J., Robinson, M. S., Becker, T. L., Weller, L. A., Edmundson, K. L., Neumann, G. A., et al. (2016). First global digital elevation model of Mercury. In *47th Annual Lunar and Planetary Science Conference* (p. 2959).

Beuthe, M. (2008). Thin elastic shells with variable thickness for lithospheric flexure of one-plate planets. *Geophysical Journal International*, *172*(2), 817–841. https://doi.org/10.1111/j.1365-246X.2007.03671.x

Beuthe, M. (2010). East–west faults due to planetary contraction. *Icarus*, *209*(2), 795–817. https://doi.org/10.1016/j.icarus.2010.04.019

Beuthe, M., Charlier, B., Namur, O., Rivoldini, A., & Van Hoolst, T. (2020). Mercury's Crustal Thickness Correlates With Lateral Variations in Mantle Melt Production. *Geophysical Research Letters*, *47*, e2020GL087261. https://doi.org/10.1029/2020GL087261

Bouley, S., Baratoux, D., Matsuyama, I., Forget, F., Séjourné, A., Turbet, M., & Costard, F. (2016). Late Tharsis formation and implications for early Mars. *Nature*, *531*(7594), 344–347. https://doi.org/10.1038/nature17171

Broquet, A. (2024). AB-Ares/Displacement_strain_planet: Version 0.5.0 (0.5.0) [Dataset]. *Zenodo*. https://doi.org/10.5281/zenodo.10552129

Broquet, A. (2025). Data for Mercury's tectonic and geodynamic history [Dataset]. *Zenodo*. https://doi.org/10.5281/zenodo.15234776

Broquet, A., & Andrews-Hanna, J. C. (2023a). Geophysical evidence for an active mantle plume underneath Elysium Planitia on Mars. *Nature Astronomy*, *7*(2), 160–169. https://doi.org/10.1038/s41550-022-01836-3

Broquet, A., & Andrews-Hanna, J. C. (2023b). Plume-induced flood basalts on Hesperian Mars: An investigation of Hesperia Planum. *Icarus*, *391*, 115338. https://doi.org/10.1016/j.icarus.2022.115338

Broquet, A., & Andrews-Hanna, J. C. (2024). The Moon before mare. *Icarus*, *408*, 115846. https://doi.org/10.1016/j.icarus.2023.115846

Broquet, A., & Andrews-Hanna, J. C. (2026). Mercury's tectonic and geodynamic history: 1. Contractional tectonic landform analysis and tectonic strain using machine learning. *Journal of Geophysical Research: Planets*, *131*, e2025JE009584. https://doi.org/10.1029/2025JE009584

Broquet, A., Maia, J., & Wieczorek, M. A. (2025). On the crustal architecture of the terrestrial planets. *Journal of Geophysical Research: Planets*, *130*(9), e2025JE009139. https://doi.org/10.1029/2025JE009139

Broquet, A., Rolser, F., Plesa, A.-C., Breuer, D., & Hussmann, H. (2024). Mercury's crustal porosity as constrained by the planet's bombardment history. *Geophysical Research Letters*, *51*(21), e2024GL110583. https://doi.org/10.1029/2024GL110583

Broquet, A., & Wieczorek, M. A. (2019). The gravitational signature of Martian volcanoes. *Journal of Geophysical Research: Planets*, *124*(8), 2054–2086. https://doi.org/10.1029/2019JE005959

Byerlee, J. D. (1978). Friction of rocks. *Pure and Applied Geophysics*, *116*(4–5), 615–626. https://doi.org/10.1007/BF00876528

Byrne, P., Klimczak, C., Celâl Şengör, A., Solomon, S. C., Watters, T. R., & Hauck II, S. A. (2014). Mercury's global contraction much greater than earlier estimates. *Nature Geoscience*, *7*(4), 301–307. https://doi.org/10.1038/ngeo2097

Campbell, I. H. (2007). Testing the plume theory. *Chemical Geology*, *241*(3–4), 153–176. https://doi.org/10.1016/j.chemgeo.2007.01.024

Crane, K. T., & Klimczak, C. (2017). Timing and rate of global contraction on Mercury. *Geophysical Research Letters*, *44*(7), 3082–3089. https://doi.org/10.1002/2017GL072711

Davies, C. J., Pommier, A., Greenwood, S., & Wilson, A. (2024). Thermal and magnetic evolution of Mercury with a layered Fe-Si(-S) core. *Earth and Planetary Science Letters*, *641*, 118812. https://doi.org/10.1016/j.epsl.2024.118812

Di Achille, G., Popa, C., Massironi, M., Mazzotta Epifani, E., Zusi, M., Cremonese, G., & Palumbo, P. (2012). Mercury's radius change estimates revisited using MESSENGER data. *Icarus*, *221*(1), 456–460. https://doi.org/10.1016/j.icarus.2012.07.005

Dombard, A. J., & Hauck, S. A. (2008). Despinning plus global contraction and the orientation of lobate scarps on Mercury: Predictions for MESSENGER. *Icarus*, *198*(1), 274–276. https://doi.org/10.1016/j.icarus.2008.06.008

Du, J., Wieczorek, M. A., & Fa, W. (2020). Thickness of lava flows within the northern smooth plains on Mercury as estimated by partially buried craters. *Geophysical Research Letters*, *47*(20), e2020GL090578. https://doi.org/10.1029/2020GL090578

Fleury, A., Plesa, A.-C., Tosi, N., Walterová, M., & Breuer, D. (2024). Variations of heat flux and elastic thickness of Mercury from 3-D thermal evolution modeling. *Geophysical Research Letters*, *51*(21), e2024GL110622. https://doi.org/10.1029/2024GL110622

Freed, A. M., Blair, D. M., Watters, T. R., Klimczak, C., Byrne, P. K., Solomon, S. C., et al. (2012). On the origin of graben and ridges within and near volcanically buried craters and basins in Mercury's northern plains. *Journal of Geophysical Research*, *117*(E12), E00L06. https://doi.org/10.1029/2012JE004119

Freed, A. M., Solomon, S. C., Watters, T. R., Phillips, R. J., & Zuber, M. T. (2009). Could Pantheon Fossae be the result of the Apollodorus crater-forming impact within the Caloris basin, Mercury? *Earth and Planetary Science Letters*, *285*(3–4), 320–327. https://doi.org/10.1016/j.epsl.2009.02.038

Genova, A., Goossens, S., Del Vecchio, E., Petricca, F., Beuthe, M., Wieczorek, M., et al. (2023). Regional variations of Mercury's crustal density and porosity from MESSENGER gravity data. *Icarus*, *391*, 115332. https://doi.org/10.1016/j.icarus.2022.115332

Goossens, S., Genova, A., James, P. B., & Mazarico, E. (2022). Estimation of crust and lithospheric properties for Mercury from high-resolution gravity and topography. *The Planetary Science Journal*, *3*(6), 145. https://doi.org/10.3847/PSJ/ac703f

Hauck II, S. A., Dombard, A. J., Phillips, R. J., & Solomon, S. C. (2004). Internal and tectonic evolution of Mercury. *Earth and Planetary Science Letters*, *222*(3–4), 713–728. https://doi.org/10.1016/j.epsl.2004.03.037

Jain, C., & Solomatov, V. S. (2024). Analysis of the cessation of convection in Mercury's mantle. *Journal of Geophysical Research: Planets*, *129*(9), e2024JE008365. https://doi.org/10.1029/2024JE008365

James, P. B., Zuber, M. T., Phillips, R. J., & Solomon, S. C. (2015). Support of long-wavelength topography on Mercury inferred from MESSENGER measurements of gravity and topography. *Journal of Geophysical Research: Planets*, *120*(2), 287–310. https://doi.org/10.1002/2014JE004713

Kennedy, P. J., Freed, A. M., & Solomon, S. C. (2008). Mechanisms of faulting in and around Caloris basin, Mercury. *Journal of Geophysical Research*, *113*(E8), E08004. https://doi.org/10.1029/2007JE002992

Klimczak, C. (2015). Limits on the brittle strength of planetary lithospheres undergoing global contraction. *Journal of Geophysical Research: Planets*, *120*(12), 2135–2151. https://doi.org/10.1002/2015JE004851

Klimczak, C., Byrne, P. K., & Crane, K. (2024). A global tectonic map of Mercury [Dataset]. *Mendeley Data V1*. https://doi.org/10.17632/p43b9wttpj.1

Klimczak, C., Byrne, P. K., & Crane, K. (2025). Mercury has multiple, superposed global tectonic patterns. *Earth and Planetary Science Letters*, *658*, 119331. https://doi.org/10.1016/j.epsl.2025.119331

Klimczak, C., Byrne, P. K., & Solomon, S. C. (2015). A rock-mechanical assessment of Mercury's global tectonic fabric. *Earth and Planetary Science Letters*, *416*, 82–90. https://doi.org/10.1016/j.epsl.2015.02.003

Knibbe, J. S., & van Westrenen, W. (2018). The thermal evolution of Mercury's Fe–Si core. *Earth and Planetary Science Letters*, *482*, 147–159. https://doi.org/10.1016/j.epsl.2017.11.006

Konopliv, A. S., Park, R. S., & Ermakov, A. I. (2020). The Mercury gravity field, orientation, love number, and ephemeris from the MESSENGER radiometric tracking data. *Icarus*, *335*, 113386. https://doi.org/10.1016/j.icarus.2019.07.020

Liang, W., Andrews-Hanna, J. C., & Evans, A. J. (2023). The missing craters and basin rings beneath the lunar maria. *Journal of Geophysical Research: Planets*, *128*(12), e2023JE007876. https://doi.org/10.1029/2023JE007876

Matsuyama, I., & Nimmo, F. (2009). Gravity and tectonic patterns of Mercury: Effect of tidal deformation, spin-orbit resonance, nonzero eccentricity, despinning, and reorientation. *Journal of Geophysical Research*, *114*(E1), E01010. https://doi.org/10.1029/2008JE003252

Ostrach, L. R., Robinson, M. S., Whitten, J. L., Fassett, C. I., Strom, R. G., Head, J. W., & Solomon, S. C. (2015). Extent, age, and resurfacing history of the northern smooth plains on Mercury from MESSENGER observations. *Icarus*, *250*, 602–622. https://doi.org/10.1016/j.icarus.2014.11.010

Peplowski, P. N., Lawrence, D. J., Rhodes, E. A., Sprague, A. L., McCoy, T. J., Denevi, B. W., et al. (2012). Variations in the abundances of potassium and thorium on the surface of Mercury: Results from the MESSENGER Gamma-Ray Spectrometer. *Journal of Geophysical Research: Planets*, *117*(E12), E00L04. https://doi.org/10.1029/2012JE004141

Phillips, R. J., Sleep, N. H., & Banerdt, W. B. (1990). Permanent uplift in magmatic systems with application to the Tharsis region of Mars. *Journal of Geophysical Research*, *95*(B4), 5089–5100. https://doi.org/10.1029/JB095iB04p05089

Plattner, A. M., & Johnson, C. L. (2021). Mercury's Northern Rise core-field magnetic anomaly. *Geophysical Research Letters*, *48*(17), e2021GL094695. https://doi.org/10.1029/2021GL094695

Solomon, S. C., McNutt, R. L., Gold, R. E., & Domingue, D. L. (2007). MESSENGER Mission overview. *Space Science Reviews*, *131*(1–4), 3–39. https://doi.org/10.1007/s11214-007-9247-6

Sori, M. (2018). A thin dense crust for Mercury. *Earth and Planetary Science Letters*, *489*, 92–99. https://doi.org/10.1016/j.epsl.2018.02.033

Thomas, N., Hussmann, H., Spohn, T., Lara, L. M., Christensen, U., Affolter, M., et al. (2021). The BepiColombo laser altimeter. *Space Science Reviews*, *217*(1), 25. https://doi.org/10.1007/s11214-021-00794-y

Tosi, N., Čadek, O., Běhounková, M., Káňová, M., Plesa, A.-C., Grott, M., et al. (2015). Mercury's low-degree geoid and topography controlled by insolation-driven elastic deformation. *Geophysical Research Letters*, *42*(18), 7327–7335. https://doi.org/10.1002/2015GL065314

Tosi, N., Grott, M., Plesa, A.-C., & Breuer, D. (2013). Thermochemical evolution of Mercury's interior. *Journal of Geophysical Research: Planets*, *118*(12), 2474–2487. https://doi.org/10.1002/jgre.20168

Tosi, N., Schulz, F., Walterová, M., & Padovan, S. (2025). The influence of spin–orbit resonances on the evolution of Mercury's mantle and crust. *Icarus*, *439*, 116630. https://doi.org/10.1016/j.icarus.2025.116630

Vasavada, A., Paige, D., & Wood, S. (1999). Near-surface temperatures on Mercury and the Moon and the stability of polar ice deposits. *Icarus*, *141*(2), 179–193. https://doi.org/10.1006/icar.1999.6175

Wang, Y., Xiao, Z., Chang, Y., Xu, R., & Cui, J. (2021). Short-term and global-wide effusive volcanism on Mercury around 3.7 Ga. *Geophysical Research Letters*, *48*(20), e2021GL094503. https://doi.org/10.1029/2021GL094503

Watters, T. R. (2021). A case for limited global contraction of Mercury. *Communications Earth & Environment*, *2*(1), 9. https://doi.org/10.1038/s43247-020-00076-5

Watters, T. R., Cook, A. C., & Robinson, M. S. (2001). Large-scale lobate scarps in the southern hemisphere of Mercury. *Planetary and Space Science*, *49*(14–15), 1523–1530. https://doi.org/10.1016/S0032-0633(01)00090-3

Watters, T. R., James, P. B., & Selvans, M. M. (2021). Mercury's crustal thickness and contractional strain. *Geophysical Research Letters*, *48*(17), e2021GL093528. https://doi.org/10.1029/2021GL093528

Weider, S. Z., Nittler, L. R., Starr, R. D., McCoy, T. J., Stockstill-Cahill, K. R., Byrne, P. K., et al. (2012). Chemical heterogeneity on Mercury's surface revealed by the MESSENGER X-Ray Spectrometer. *Journal of Geophysical Research: Planets*, *117*(E12), E00L05. https://doi.org/10.1029/2012JE004153

Wieczorek, M., Correia, A. C. M., Le Feuvre, M., Laskar, J., & Rambaux, N. (2012). Mercury's spin–orbit resonance explained by initial retrograde and subsequent synchronous rotation. *Nature Geoscience*, *5*(1), 18–21. https://doi.org/10.1038/ngeo1350

Williams, J. P., Ruiz, J., Rosenburg, M. A., Aharonson, O., & Phillips, R. J. (2011). Insolation driven variations of Mercury's lithospheric strength. *Journal of Geophysical Research: Planets*, *116*(E1), E01008. https://doi.org/10.1029/2010JE003655

Zuber, M. T., Smith, D. E., Phillips, R. J., Solomon, S. C., Neumann, G. A., Hauck II, S. A., et al. (2012). Topography of the Northern Hemisphere of Mercury from MESSENGER laser altimetry. *Science*, *336*(6078), 217–220. https://doi.org/10.1126/science.1218805